Progress In Electromagnetics Research M, Vol. 71, 19–29, 2018

Comparative Study of IPM Synchronous Machines with Different Saliency Ratios Considering EVs Operating Conditions

Wenye Wu, Xiaoyong Zhu*, Li Quan, Yifeng Hua, and Qing Lu

Abstract—In this paper, based on different saliency ratios ρ, three interior permanent magnet (IPM) synchronous machines respectively owning a large ρ, a low ρ and an inverse ρ are proposed for the potential applications of electrical vehicles (EVs). To grasp the impacts of saliency ratio on machine performances, comparative studies are conducted at low speed operation (constant torque region) and high speed operation (constant power region), respectively. In particular, the overload capability referring to magnet demagnetization is emphasized in low-speed heavy-duty operation region. And in high speed, the constant power speed range (CPSR) and high efficiency range are investigated. The main results put in evidence the different behaviors of the three machines in terms of EVs operating conditions. Though all three machines reveal considerable behaviors in CPSR, the inverse saliency ratio machine shows a larger high efficiency region and extends the high efficiency region to a wider speed-and-torque range due to its unique characteristic of $L_q < L_d$.

1. INTRODUCTION

Automotive industry applications are oriented increasingly toward more energy-efficient and environmentally friendly drive-train technologies. This trend is mainly attributed to the detrimental effects of greenhouse gas emissions caused by vehicle emissions. Thus, the diffusion of pollution-free electric cars in urban environment will become an irreversible trend in the near future. However, as one of the vital components in electrical vehicles (EVs), the choice of electric drive-train most suited for EVs application is still a matter of discussions [1–3].

Nowadays, due to high torque density, high efficiency, high reliability and mass saving, permanent magnet synchronous machines have become attractive candidates for EVs drive systems [1–5]. In particular, as a representative of conventional permanent magnet machine, surface PM (SPM) machine is widely used for its simple construction and short end connections. However, this type of machine exhibits no magnetic saliency (i.e., $L_d = L_q$) so that there is no reluctance torque can be used. As a result, the overload capacity and speed regulation capability are relatively restricted in multi-driving cycles of EVs [4].

Figure 1 illustrates the typical torque/power-speed characteristics of an EV needed PM machine. In general, EVs require a constant-torque performance at low speed and a constant-power region at high speed. In addition, the high efficiency is extremely desired in entire speed region [5, 6]. Hence, to achieve these particular requirements, interior permanent magnet (IPM) machines with characteristic of $L_d \neq L_q$ have been explored in the past years. In [7–9], large saliency ratio (i.e., $L_q \gg L_d$) machines named permanent magnet assisted synchronous reluctance (PMASR) machines are studied, where the PM quantity is designed sufficiently low, and reluctance torque dominates in torque production. On the other hand, another type of IPM machines, generally called flux intensifying IPM machines, has also

Received 30 May 2018, Accepted 12 July 2018, Scheduled 24 July 2018
* Corresponding author: Xiaoyong Zhu (zxyff@ujs.edu.cn).
The authors are with the Department of School of Electrical and Information Engineering, Jiangsu University, Zhenjiang 212013, China.

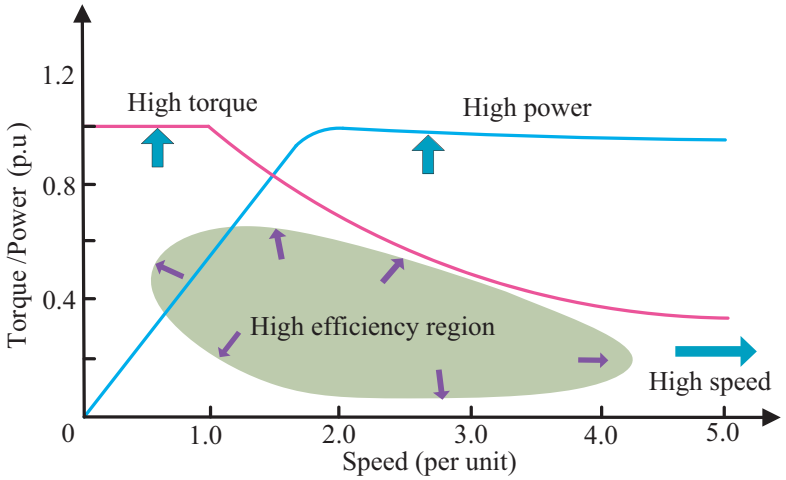

Figure 1. Application requirements of EVs machines.

been proposed for the EVs traction applications [10, 11]. In these machines, the d-axis inductance is raised sufficiently high that L_d is greater than L_q, corresponding to the inverse condition of the typical interior PM machines. Both machines with $L_q > L_d$ and $L_q < L_d$ have revealed unique advantages in heavy load conditions and CPSR operations.

Currently, some articles have reported the design of machines under different operating conditions [12–15]. In [12], the dynamic behaviors of a permanent magnet synchronous machine are investigated in which three different operation conditions such as no load, rated operation, and short circuit are analyzed. In [13] and [14], by considering the limitation of different load current, the robustness against demagnetization of an ferrite assisted synchronous reluctance machine is studied, and the investigations show that the larger machines have more risk of demagnetization than smaller ones when overload current is applied. In [15], the optimization design of PM synchronous machines is performed to reduce the losses in high speed operation condition, and the methods enlarging operating efficiency especially in high speed light load region are proposed. In summary, the operation characteristics of machines in various operating conditions have been studied extensively. Yet, the above researches are more concerned on the design or optimization design of machines under multiple operating conditions, and few researches have discussed the influence of rotor saliency ratio on the design of PM machines in various EVs operating conditions.

In this paper, by different combinations of PM pieces and flux barriers in machine rotors, three types of IPM machines respectively with large saliency ratio ($L_q \gg L_d$), low saliency ratio ($L_q > L_d$) and inverse saliency ratio ($L_q < L_d$) are designed for the potential applications in EVs. Based on it, a comparative study on the three machines is carried out to clarify the influence of saliency ratio on the different operation conditions of machines especially in constant torque region and constant power region. The relevant conclusions will be given at the end of this article.

2. MACHINE DESIGN AND OPERATION CHARACTERISTICS

2.1. Machine Design

Generally, the basic equation for torque in the d-q synchronous reference frame can be described as

$$T = \frac{3}{2} p \left(\lambda_{pm} + (L_d + L_q) i_d\right) i_q \tag{1}$$

where T is the output torque; p is the pole pair number; λ_{pm} is the flux linkage produced by magnets in the d-axis; L_d and L_q are the inductance in the d- and q-axes, respectively; i_d and i_q are current vectors in the d-axis and q-axis, respectively.

It can be noted in Equation (1) that the torque production in an IPM machine combines two components. One is a magnet torque component caused by magnets in the rotor, and the other is

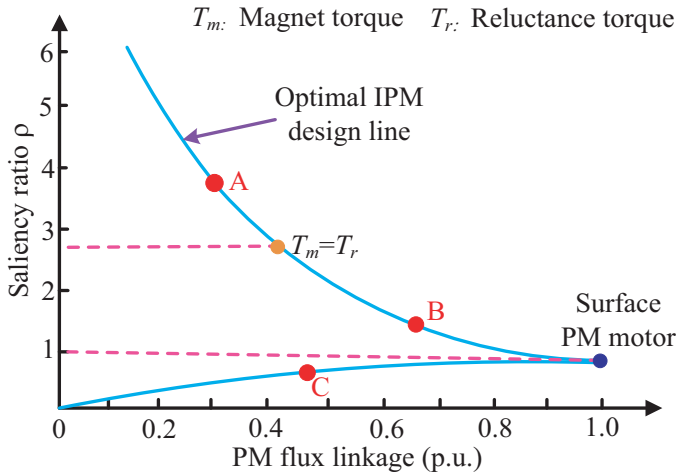

Figure 2. Selection of design points based on saliency ratio and PM flux linkage.

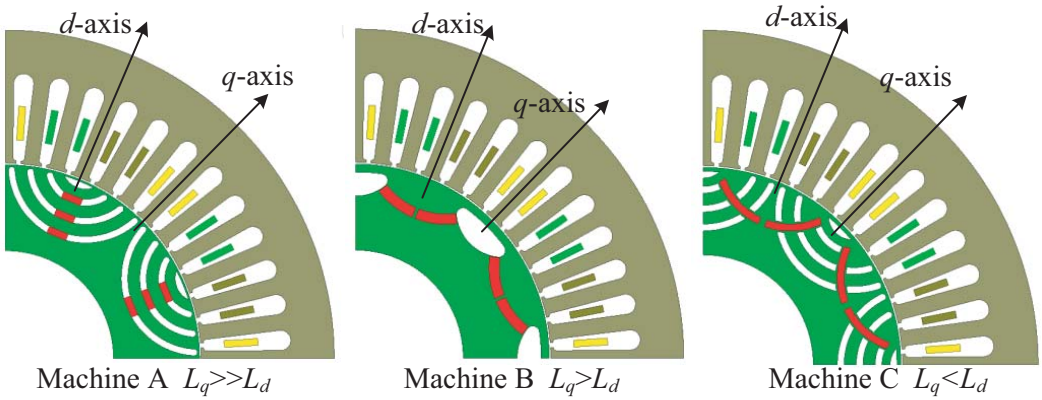

Figure 3. The three proposed machines.

a reluctance torque component generated by a rotor anisotropy structure. The choice of the relative proportion of the two components represents a tradeoff between the magnet quantity and the realization of a high anisotropic rotor structure [16, 17]. As shown in Fig. 2, all potential IPM machines with different combinations of magnet torque and reluctance torque can be depicted in a region determined by the saliency ratio (L_q/L_d) and PM flux linkage. Here, three design points of A, B, and C respectively represent a large saliency ratio, a low saliency ratio and an inverse saliency ratio which are chosen in the optimal machine combination lines. Based on it, three machines are designed as shown in Fig. 3.

In the case of design A, four layers of flux barriers are set in its d-axis to result in a large inductance difference between L_q and L_d, i.e., a large saliency ratio. Meanwhile, a small amount of magnets is inserted to the flux barriers to produce an assisted torque. As for machine B, arc-shaped magnets are arranged separately in its d-axis to ensure the mechanical strength of rotor. Since magnetic permeability of the magnet in d-axis is almost equal to the air cavities in q-axis, a relatively low saliency can be realized. In machine C, multilayer flux barriers are set in the q-axis magnetic flux path to suppress the q-axis magnetic flux, so as to produce a small L_q, and meanwhile thin arc-shaped magnets are adopted to enhance L_d. Thus, an inverse saliency ratio machine is constructed, where the inductance of L_d is larger than L_q.

The specific machine parameters are shown in Table 1. For fair comparison, the same stator structure and winding layout are applied in the three machines. The only difference is the structure of the rotor, including the placement of permanent magnets and the setting of magnetic barriers. The material used for the rotor and stator is cold rolled unoriented silicon steel sheet of 50W360. Compared

Table 1. Main design specifications of the three machines.

Parameters	Machine A	Machine B	Machine C
Rated power (kW)	5.0	←	←
Rated speed (rpm)	1200	←	←
Rated torque (Nm)	42	←	←
Stator lamination OD (mm)	192	←	←
Stator lamination ID (mm)	116	←	←
Rotor lamination OD (mm)	115	←	←
Rotor lamination ID (mm)	64	←	←
Stator and rotor stack length (mm)	65	←	←
Stack factor	0.94	0.94	0.94
Stator core mass (kg)	6.8	6.8	6.8
Rotor core mass (kg)	2.72	2.94	2.66
Number of turns	16	←	←
PM property	NdFeB (1.2 T)	NdFeB (1.2 T)	NdFeB (1.2 T)
PM quantity (mm^3)	15600	34320	32656

with hot-rolled silicon steel, the material of 50W360 has a uniform thickness and a smooth surface, thus the filling coefficient and magnetic energy of the material can be improved. Besides, the relatively low iron loss and high magnetic induction characteristics of the material are conducive to the improvement of motor efficiency.

2.2. Operation Characteristics

To clarify the operation characteristics of the machines with different saliency ratios, the vector diagrams of the three machines are drawn in Fig. 4. As for the cases of machine A and machine B, since their L_q is larger than L_d, both of them operate in flux weakening state when maximum torque per ampere (MTPA) control strategy is applied below rated speed. However, it should be pointed that in machine B, the flux linkage of λ_r produced by the stator current is slightly rotated from the current vector i_s (meaning a poor saliency), hence a large λ_m contribution is needed for obtaining sufficient torque. On the other hand, in machine A, the PM flux linkage is much lower so that a relatively low weakening

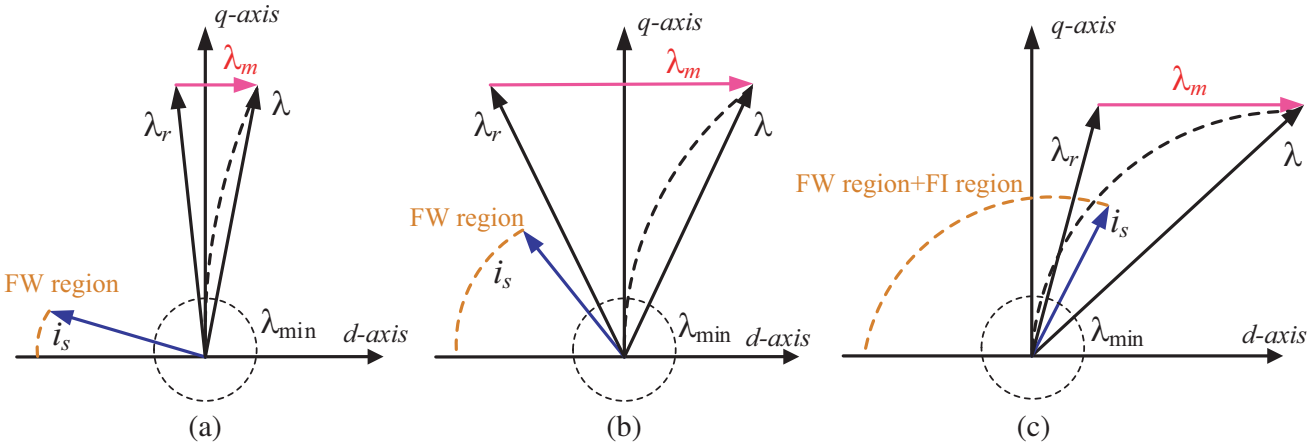

Figure 4. Vector diagrams of the three machines. (a) Machine A. (b) Machine B. (c) Machine C.

current i_d is enough to offset the PM flux linkage λ_m to its minimum value of $\lambda_{\min}$. As for machine C, due to the characteristic of inverse saliency ratio, current vector i_s is located in the first quadrant, leading to operation with magnetizing d-axis current, which is a condition that is not common with machines of $L_q > L_d$. Thus, the machine with inverse saliency ratio has a better use of magnet since it applies negative d-axis current only at high speed while the normal saliency PM machines of A and B need to weaken the magnet flux in the whole speed range.

3. LOW SPEED AND HEAVY DUTY PERFORMANCES

As known, large power and torque are often required for EVs heavy load applications. Besides, depending on inverter size, the peak torque can be two or even three times the rated torque when operating in start condition, acceleration condition or climbing with heavy load condition. To evaluate different machine designs in low speed performances, finite-element analyses (FEA) are performed using the software of Maxwell.

Once the rotor of the three IPM synchronous machines are determined with respect to the saliency ratio design rules, the PM operating points can be evaluated at I_d load conditions especially at the limit of irreversible demagnetization [18, 19]. In other words, in constant torque region, no matter light load or heavy load is required, the operating point of permanent magnet must stay above the irreversible demagnetization limit of B_{knee} as shown in Fig. 5. In general, the no load flux density of the PM (B_{nl}) which implicitly depends on the desired air gap flux density is computed by a given PM dosage. Since the permanent magnet dosages of the three machines are approximately the same, the machine's irreversible demagnetization will be determined by the magnitude of the demagnetizing current. Therefore, when the rated current and overload current are applied, the operation point of the PM under rated load and over load can be achieved. The operating points of B_{rl} and B_{ol} are compared with the knee point flux density B_{knee} in order to check the PM demagnetization.

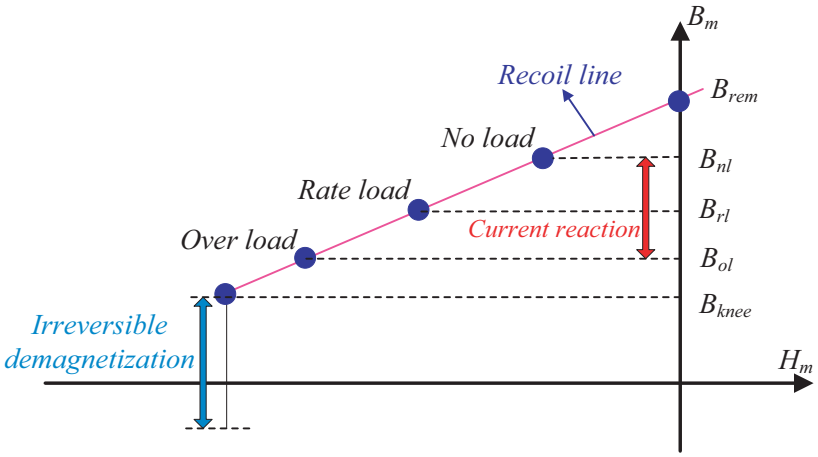

Figure 5. Demagnetization curve of the PM under different operating conditions.

Here, the overload operation is considered with two times of rated current. Fig. 6 is the schematic diagram of magnet working state in the three machines when overload current is applied. As shown, the magnet operating point of P_0 corresponding to the no-load state is located in the intersection of load line and recoil line. As overload is needed, the field intensifying current (positive i_d) is applied to machine C, and field weakening current is applied to machine A and machine B, hence the magnet working point of machine C is above the no-load point, and the magnet operating points of machine A and B are located below the no-load point. Once the weakening current $-i_d$ exceeds a certain value, the magnet operating points may be close to the demagnetization point of (F_k, Φ_k), which is undesired for EVs overload applications.

In order to further clarify the operation characteristics of the three machines in overload condition, simulations referring to flux density distributions are conducted in twice rated current of 80 A. It can

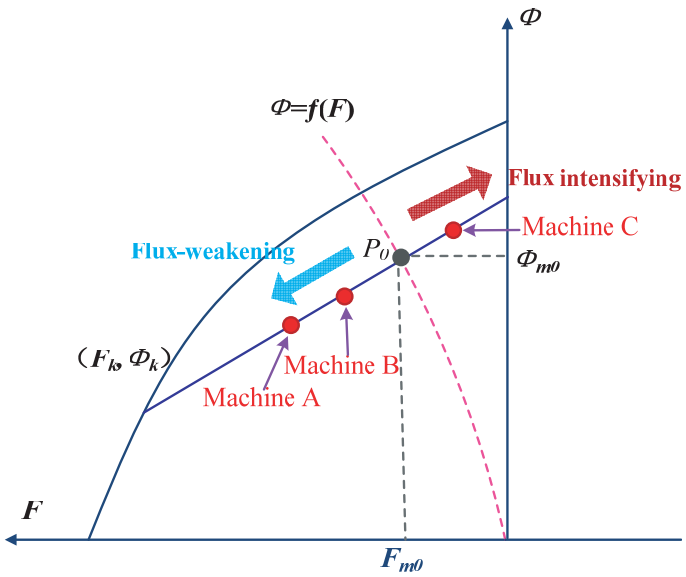

Figure 6. Schematic diagram of magnet working state in the three machines under overload current.

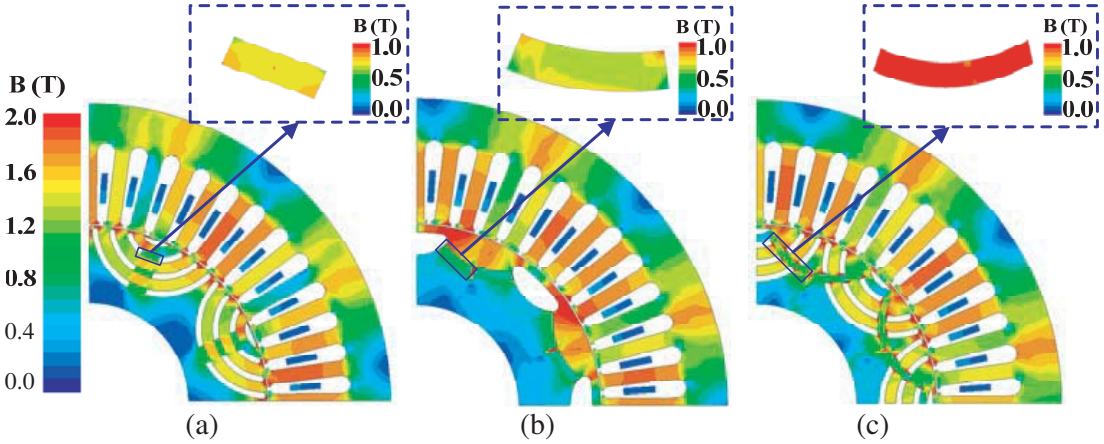

Figure 7. Flux density distributions at the same rotor position under overload current of 80 A. (a) Machine A. (b) Machine B. (c) Machine C.

be seen from Fig. 7 that due to the flux-intensifying characteristic of $L_q < L_d$, the magnet flux density in machine C is higher than the corresponding magnets in machine A and machine B. For better presentation, taking the magnet center as observation points, the detailed variations of magnet flux density versus rotor position of the three machines are investigated, and the results are shown in Fig. 8. From the figure, it can be observed that the magnet flux density of machine C is substantially greater than those in machines A and B. It indicates that a lower risk of irreversible demagnetization in machine C can be obtained even the machine operates in an overload operation condition of maximum peak torque.

4. HIGH SPEED PERFORMANCES

4.1. CPSR Capability

Serving as a traction component in EVs, the machine is regarded as the heart of the EVs. The wide speed range is a vital standard to evaluate the performance of the traction machine, so investigation on

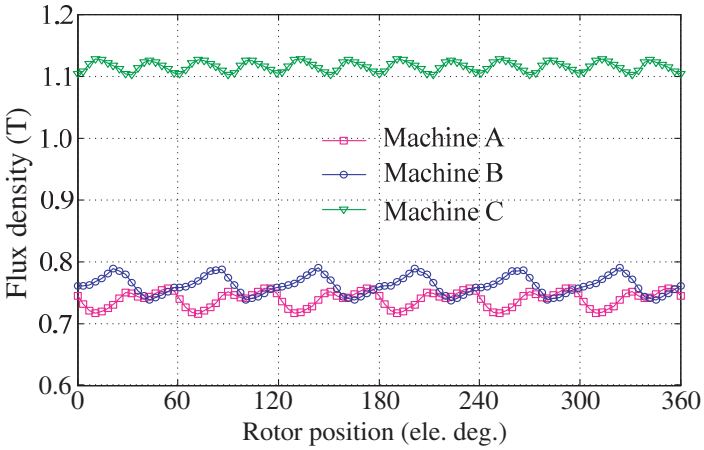

Figure 8. Flux density variations of observation PM points of the three machines at different rotor positions.

the flux-weakening capability and the capability of *CPSR* with the variation of the speed is necessary.

Without considering the effect of saturation and loss, the speed equation can be expressed as:

$$\omega_s = \frac{v_s}{\sqrt{(L_d i_d + \lambda_m)^2 + (L_q i_q)^2}} \tag{2}$$

where the definitions of i_d, i_q, L_d, L_q and λ_m are same as above, and ω_s is the rotor speed.

In practice, during flux-weakening operations, the armature reaction modifies the saturation level of the machines and makes the machine parameters variable. In fact, the saturation level mainly related to the current angle β and d- and q-axis flux linkages can be considered as the functions of β. Hence, the speed and torque equations with the saturation effect can be rewritten as:

$$\omega_s = \frac{v_s}{\sqrt{(\lambda_d(\beta))^2 + (\lambda_q(\beta))^2}} \tag{3}$$

$$T = \frac{3}{2} p i_s [\lambda_d(\beta)\cos(\beta) + \lambda_q(\beta)\sin(\beta)] \tag{4}$$

In constant torque region, the corresponding peak torque $T_{\max}$ can be obtained by solving $dT/d\beta = 0$. Hence, the base speed can be achieved as

$$\omega_{rated} = \frac{v_s}{\sqrt{\lambda_d(\beta_{T\max})^2 + \lambda_q(\beta_{T\max})^2}} \tag{5}$$

In constant power region, the corresponding maximum speed $\omega_{\max}$ is

$$\omega_{\max} = \frac{v_s}{\sqrt{\lambda_d(\beta_2)^2 + \lambda_q(\beta_2)^2}} \tag{6}$$

where β_2 is achieved by solving the power equation when the power goes below its rated value in flux-weakening regions.

Therefore, the CPSR capability for IPM synchronous machines can be defined as [20, 21]:

$$CPSR = \frac{\omega_{\max}}{\omega_{rated}} = f(\lambda_d(\beta), \lambda_q(\beta)) = f(L_d(\beta), L_q(\beta), \lambda_m) \tag{7}$$

where $L_d(\beta)$ and $L_d(\beta)$ are the d-axis and q-axis inductances with the effect of machine saturation. Therefore, it is drawn that the CPSR capability has a great relationship with the parameters of d-axis inductance, q-axis inductance and PM flux linkage.

Figure 9 shows the inductance characteristics and flux linkage characteristics of the three machines. It is found from Fig. 9(a) that all three machines are able to maintain their constant saliency ratio in flux weakening region, in which machine C owns the highest L_d, meaning that machine C can operate

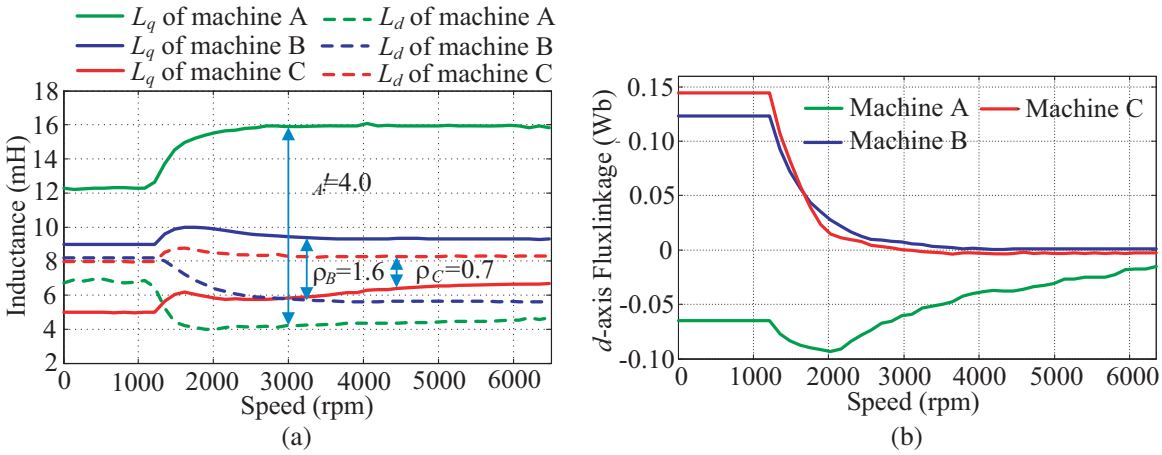

Figure 9. Inductance and flux linkage characteristics. (a) Inductance versus speed. (b) d-axis flux linkage versus speed.

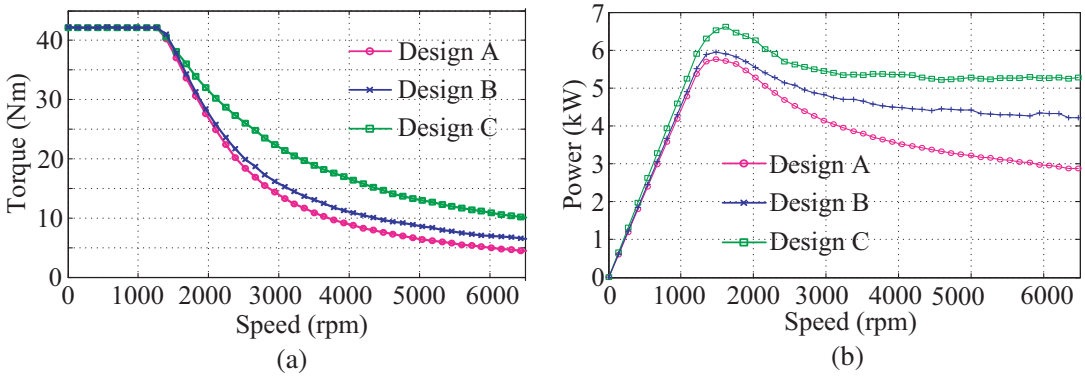

Figure 10. Torque-speed and power-speed characteristics. (a) Torque-speed envelops. (b) Power-speed envelops.

up to a high speed only with a small amount of i_d. Fig. 9(b) shows the variations of d-axis flux linkage versus speed. In the case of machine A, due to a very large saliency ratio, the d-axis flux linkage is negative in the whole operation region, that is, $L_d i_s$ is larger than λ_m. It means that machine A will operate with a reduced current once current limit is reached. Consequently, peak constant power can be hardly maintained in high speed region. Instead, both machine B and machine C can achieve the condition of $\psi_m = L_d i_s$, which is expected to be advantageous to keep a constant output power at high speed operation.

Figure 10 shows the torque and output power capabilities of the three investigated machines, where the rated speed of the three machines is 1200 rpm, and the rated current is the same. It can be seen from the torque-speed curves shown in Fig. 10(a) that all three machines realize the speed range of 6000 rpm (5 times rated speed). However, it is worth noting that machine C can maintain torque output approximately at 10 Nm when the speed reaches 6000 rpm, which is higher than the torque values in the other two machines. It indicates that speed range of machine C is expected to extend to a higher level. Besides, from the power-speed envelops shown in Fig. 10(b), we can observe that machine C can get nearly constant power until 6000 rpm, but machine A and machine B cannot achieve it.

4.2. Efficiency Analysis

In this section, the efficiency maps of the three machines are evaluated by FEA, and the results are shown in Fig. 11. Since the same rated current is applied in all the three machines, it is found that

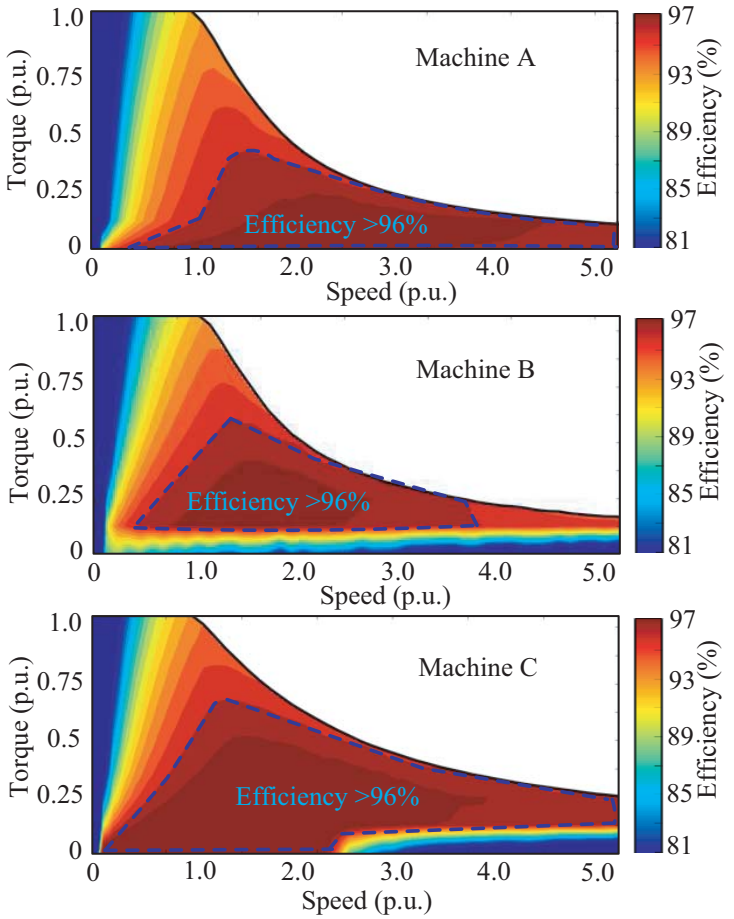

Figure 11. Efficiency characteristics by FEA.

efficiency is almost same in low speed region. On the other hand, when the focus shifts to high speed region, the behaviors of efficiency maps reveal a large difference. In fact, all three machines can reach the maximum efficiency value of 96%. However, the 96% region is limited to less than 4 times rated speed for machine B because of the increased iron loss and copper loss in high speed. In addition, though both machine A and machine C can maintain the 96% efficiency to their 5 times rated speed, machine C presents a wider high efficiency region, and its high efficiency also extends to a larger torque region. Therefore, it can be achieved that machine C can operate with a higher load in medium-to-high speed, which is extremely advantageous for EVs acceleration in high speed operation.

5. CONCLUSION

In this paper, based on different saliency ratios ρ, three interior permanent magnet synchronous machines respectively owing large ρ, low ρ and inverse ρ are proposed for the potential applications of EVs. Comparative studies are conducted at low speed operation (constant torque region) and high speed operation (constant power region). Results indicate that machine C with inverse saliency ratio shows higher performances not only in constant torque region, but also in constant power region. In particular, a better ability to resist demagnetization is achieved when overload current is applied in low speed driving. In addition, the inverse saliency ratio machine shows a larger high efficiency region and extends the high efficiency region to a wider speed range and high torque region.

ACKNOWLEDGMENT

This work was supported in part by the National Natural Science Foundation of China under Grant 51377073, 51477069 and 51777089, in part by the Priority Academic Program Development of Jiangsu Higher Education Institutions, and in part by the Project of Innovation of Postgraduate of Jiangsu Province of KYZZ16_0335.

REFERENCES

1. ChauK. T., C. Chan, and C. Liu, "Overview of permanent-magnet brushless drives for electric and hybrid electric vehicles," *IEEE Trans. Ind. Electron.*, Vol. 55, No. 6, 2246–2257, 2008.
2. Refaie, A. E., "Motors/generators for traction/propulsion applications: A review," *IEEE Veh. Technol. Mag.*, Vol. 8, No. 1, 90–99, 2013.
3. Zhu, X. Y., Z. Shu, L. Quan, Z. Xiang, and X. Pan, "Design and multi-condition comparison of two outer-rotor flux-switching permanent magnet motors for in-wheel traction applications," *IEEE Trans. Ind. Electron.*, Vol. 64, No. 8, 6137–6148, 2017.
4. Pellegrino, G., A. Vagati, P. Guglielmi, and B. Boazzo, "Performance comparison between surface-mounted and interior PM motor drives for electric vehicle application," *IEEE Trans. Ind. Electron.*, Vol. 59, No. 2, 803–811, 2012.
5. Sarigiannidis, A. G., M. Beniakar, and A. Kladas, "Fast adaptive evolutionary PM traction motor optimization based on electric vehicle drive cycle," *IEEE Trans. Veh. Technol.*, Vol. 66, No. 7, 2017.
6. Zhu, X. Y., Z. Xiang, L. Quan, W. Wu, and Y. Du, "Multi-mode optimization design methodology for a flux-controllable stator permanent magnet memory motor considering driving cycles," *IEEE Trans. Ind. Electron.*, Vol. 65, No. 7, 5353–5366, Jul. 2017.
7. Masahiro, O., M. Shigeo, S. Masayuki, and I. Yukinori, "Performance of PMASynRM with ferrite magnets for EV/HEV applications considering productivity," *IEEE Trans. Ind. Appl.*, Vol. 50, No. 4, 2427–2435, 2014.
8. Ooi, S., S. Morimoto, M. Sanada, and Y. Inoue, "Performance evaluation of a high-power-density PMASynRM with ferrite magnets," *IEEE Trans. Ind. Appl.*, Vol. 49, No. 3, 1308–1315, 2014.
9. Bianchi, N., M. Fornasiero, and W. Soong, "Selection of PM flux linkage for maximum low-speed torque rating in a PM-assisted synchronous reluctance machine," *IEEE Trans. Ind. Appl.*, Vol. 51, No. 5, 3600–3608, 2015.
10. Limsuwan, N., T. Kato, K. Akatsu, and R. Lorenz, "Design and evaluation of a variable-flux flux intensifying interior permanent magnet machine," *IEEE Trans. Ind. Appl.*, Vol. 50, No. 2, 1015–1024, 2014.
11. Limsuwan, N., Y. Shibukawa, D. Reigosa, and R. Lorenz, "Novel design of flux-intensifying interior permanent magnet synchronous machine suitable for self-sensing control at very low speed and power conversion," *IEEE Trans. Ind. Appl.*, Vol. 47, No. 5, 2004–2012, 2011.
12. Kamiev, K., J. Montonen, M. Ragavendra, J. Pyrhönen, J. Tapia, and M. Niemelä, "Design principles of permanent magnet synchronous machines for parallel hybrid or traction application," *IEEE Trans. Ind. Electron.*, Vol. 60, No. 11, 4881–4890, 2013.
13. Alfredo, V., B. Barbara, G. Paolo, and P. Gianmario, "Design of ferrite-assisted synchronous reluctance machines robust toward demagnetization," *IEEE Trans. Ind. Appl.*, Vol. 50, No. 3, 1768–1779, 2014.
14. Paolo, G., B. Barbara, A. Eric, P. Gianmario, and V. Alfredo, "Permanent-magnet minimization in PM-assisted synchronous reluctance motors for wide speed range," *IEEE Trans. Ind. Appl.*, Vol. 49, No. 1, 31–41, 2013.
15. Degano, M., E. Carraro, and N. Bianchi, "Selection criteria and robust optimization of a traction PM-assisted synchronous reluctance motor," *IEEE Trans. Ind. Appl.*, Vol. 51, No. 6, 4383–4391, 2015.

16. Soong, W. L. and T. Miller, "Field-weakening performance of brushless synchronous AC motor drives," *IEEP Elec. Power Appl.*, Vol. 141, No. 6, 331–340, 1994.
17. Wu, W. Y., X. Zhu, L. Quan, Y. Du, Z. Xiang, and X. Zhu, "Design and analysis of a hybrid permanent magnet assisted synchronous reluctance motor considering magnetic saliency and PM usage," *IEEE Appl. Supercond.*, Vol. 28, No. 3, 1–6, 2017.
18. Nicola, B. and M. Hanafy, "An analytical approach to design the PM in PMAREL motors robust toward the demagnetization," *IEEE Trans. Energy Convers.*, Vol. 31, No. 2, 800–809, 2016.
19. Wu, W. Y., X. Zhu, L. Quan, D. Fan, and Z. Xiang, "Characteristic analysis of a less-rare-earth hybrid PM-assisted synchronous reluctance motor for EVs application," *AIP Advances*, Vol. 7, No. 5, 1–6, 2017.
20. Huynh, T. A. and M. F. Hsieh, "Comparative study of PM-assisted SynRM and IPMSM on constant power speed range for EV applications," *IEEE Trans. Magn.*, Vol. 53, No. 11, 2017.
21. Jolly, L., M. Jabbar, and Q. Liu, "Optimization of the constant power speed range of a saturated permanent-magnet synchronous motor," *IEEE Trans. Ind. Appl.*, Vol. 42, No. 4, 1024–1030, 2006.